Full length article

Mechanical performance and design optimisation of metal honeycombs fabricated by laser powder bed fusion

Shahriar Afkhami [a,*], Mohsen Amraei [b,d], Leroy Gardner [c], Heidi Piili [d], M. Ahmer Wadee [c], Antti Salminen [d], Timo Björk [a]

[a] Laboratory of Steel Structures, LUT University, Lappeenranta, 53850, Finland
[b] Laboratory of Laser Materials Processing and Additive Manufacturing, LUT University, Lappeenranta, 53850, Finland
[c] Department of Civil and Environmental Engineering, Imperial College London, London, UK
[d] Department of Mechanical and Materials Engineering, University of Turku, Turku, 20520, Finland

A B S T R A C T

Honeycomb structures have a wide range of applications, from medical implants to industrial components. In addition, honeycombs play a critical role when passive protection is required due to their low density and high energy absorption capabilities. With the transition of additive manufacturing from a rapid prototyping approach to a manufacturing process, this technology has recently offered designers and manufacturers the ability to fabricate and modify lattice structures such as honeycombs. The current study presents the application of laser powder bed fusion, a common additive manufacturing process for producing industrial metal components, for fabricating metal honeycombs. In addition, this study examines three modified designs that can only be practically fabricated using additive manufacturing and compares them with conventional honeycombs. For this purpose, quasi-static and dynamic compression tests are conducted to evaluate and compare the performance of the honeycomb structures. The results show that the structures produced by additive manufacturing have acceptable performance compared to conventional honeycomb structures, and laser powder bed fusion can be considered to be a reliable manufacturing method for honeycomb production. Furthermore, the honeycombs produced according to the modified designs generally outperformed their counterparts made from the typical hexagonal cells. Ultimately, the use of triangular cells as a design modification is proposed to produce honeycombs with promising performance characteristics in all of their principal axes and under various pressure scenarios, from quasi-static to dynamic loading rates. Finally, this study also investigates the applicability of a newly developed maraging steel for additive manufacturing of honeycombs. Microstructural analysis and quasi-static tensile tests have confirmed the material properties for this purpose.

1. Introduction

Additive manufacturing (AM) is the process of building solid components from digital models by adding material layer by layer. This technology has evolved during the last decade from a rapid prototyping approach to a manufacturing method. The development and application of AM as a manufacturing technique offer large potential for waste reduction, more sustainable production, enhanced design freedom, and new ranges of material properties as per the expected applications [1–5]. The unprecedented design freedom that AM offers for designers has led to the emergence of a new subcategory known in the nomenclature of mechanical design as 'design for additive manufacturing' (DfAM). In addition, laser powder bed fusion (L-PBF) is commonly used among the various AM techniques to fabricate metal components

because of its ability to produce fully dense metal parts with complex geometries accurately. In summary, leveraging the simultaneous advantages of DfAM and L-PBF makes optimisation of conventional designs feasible. Furthermore, utilising these advantages enables the design and manufacture of parts that would be impossible to produce using conventional manufacturing methods [6,7].

Thin-walled metal structures, including honeycombs, offer designers a favourable combination of low cost and high energy absorption capability among the various structures and components that can be redesigned and modified with DfAM. In particular, honeycomb structures can absorb or dissipate the initial kinetic energy from external mechanical loads in a controlled manner [8]. Consequently, the applications of honeycomb structures typically involve loading scenarios featuring compressive or impact loads. These thin-walled structures

are frequently used in the automotive and aviation industries, where novel solutions to safety issues are always in demand [1,2,9,10]. In addition, honeycomb structures are regularly used in aerospace applications since their structural components require a very high stiffness to weight ratio under compression or bending. For example, critical mass reduction is essential for satellites due to their payloads and operating costs [3,9,11]. Honeycomb structures can also be used in passive protection systems for military vehicles, rapid public transportation systems, critical infrastructure elements, and cores of sandwich panels to make them more resistant to bending and buckling [12,13]. Additionally, these structures have recently been considered to be used as porous scaffolds for tissue regeneration in medical implants [10]. Honeycomb structures are also used as thermal, acoustic and vibration insulators [14].

Conventional metallic honeycombs are typically made by cold expansion of periodically bonded metal strips or by adhesive bonding or welding corrugated metal sheets. Consequently, conventional honeycomb structures suffer from localised irregular geometries, adhesive bonds or welds that act as potential weak points, operating temperatures limited to the working temperature of adhesive agents, and lack of design flexibility owing to the limitations of conventional manufacturing processes [15]. In contrast with conventionally manufactured honeycombs, those fabricated by AM processes, in particular L-PBF, have regular geometries and do not require adhesives. In addition, honeycomb structures made using L-PBF can have constant wall thicknesses throughout their structure, while conventionally manufactured honeycomb structures usually have a half-wall thickness along their outer walls or a double-wall thickness for their vertical cell walls owing to their manufacturing process limitations [13]. L-PBF honeycombs also have shorter time intervals from design to fabrication than conventionally manufactured honeycomb structures and can be directly manufactured into a near-net shape [14].

Studies on L-PBF honeycombs are limited in number and scope. According to these studies, nonuniform energy absorption capacities and anisotropic microstructures are some of the potential issues associated with AM honeycomb structures compared to conventionally manufactured ones, as AM honeycomb structures have relatively inferior geometrical properties, dimensional accuracies, and surface qualities. [10,15,16]. Furthermore, the reliability of equations used for conventional honeycombs, e.g., those attributed to Gibson et al. [17], Wierzbicki [18], or Zhang and Ashby [19], applied to AM honeycombs is of interest since metals processed by AM typically suffer from defects inherent to this technology, such as porosity [7,20]. For example, defects can significantly affect the elastic properties of lattice structures, including honeycombs, and potentially decrease their apparent elastic or tangent modulus. Therefore, defects reduce the stress required for plastic collapse and cause deviations from standard numerical approaches [16]. Although honeycombs can provide a good combination of low density and high stiffness, these properties depend on their cell shape and wall thickness [10,16]. Considering the design freedom associated with AM, studies such as [9] included triangular cells as a novel design for honeycombs to improve their performance. However, triangular honeycombs were only analysed via the finite element approach (FE) in [9]. In another study, DfAM was successfully used to convert honeycombs into auxetic structures by changing their cell design [11].

Considering the vast potential applications of AM honeycombs and the high dependency of their mechanical performance, as crashworthy structures, for instance, on cell size and cell design, the present study aims to investigate the effects of these parameters on the mechanical properties and crashworthiness of honeycombs manufactured by L-PBF. To address some noteworthy gaps in the literature, both out-of-plane and in-plane compressive loads are considered presently to obtain a comprehensive understanding of the mechanical behaviour of the honeycombs along all principal axes. In addition to the quasi-static loads, the honeycombs have also been subjected to high-velocity impacts to

Table 1
Nominal chemical composition of the raw powder [27].

Element	Fe	Cr	Ni	Mo	Al	Mn	Si	C
Max wt%	Bal.	13.00	10.00	1.700	2.000	0.400	0.400	0.050
Min wt%	Bal.	11.00	8.400	1.100	1.200	–	–	–

compare their mechanical behaviour during such loads. Furthermore, three modified designs are compared to conventional hexagonal designs to investigate the role of DfAM in improving their performance. The modified designs comprise triangular or diamond-shaped cells instead of hexagons. Finally, since the applicability of honeycombs mainly relies on their materials and cell designs, a recently developed steel known as CX is used in the L-PBF process (hereafter abbreviated as L-PBF CX) [14]; L-PBF CX appears to be a suitable replacement for more expensive alloys such as Ti6Al4V, especially in aerospace applications, owing to its relatively lower cost alongside a favourable combination of strength, ductility, corrosion resistance and heat treatability [21–26].

2. Materials and methods

Fresh gas-atomised stainless tool steel powder with a Cr content of 13 wt% was used in this study as the raw material. The powder was purchased from EOS GmbH and is known commercially as CX. The chemical composition of the alloy is given in Table 1. The samples were fabricated using an EOS M 290 machine equipped with a Yb fibre laser comprising a maximum output of 400 W, a wavelength of 1070 nm and a focal point diameter of 100 μm. The fabrication parameters are given in Table 2. Six different designs were selected for this study and are shown in Fig. 1. Three original designs (labelled A, B, and C) comprised hexagonal cells with different cell sizes for each design. These designs were considered to investigate the effect of cell size on the mechanical response of honeycomb structures to external loads and impacts.

In addition to the original designs, three modified designs (labelled D, E, and F) were considered to investigate how the addition of internal walls (reinforcements) affects the behaviour of the structures when loaded in different directions. In design D, the intersections of the cell walls and the internal reinforcements are located in the middle of the cell walls, resulting in a honeycomb structure with diamond-shaped elements. In design E, the intersections are located at the corners of the cells, resulting in a honeycomb structure with triangular elements. Finally, design F is similar to design D, but the internal reinforcements are gently curved in height to increase the bending moment required for the internal walls to fail. These modified designs are also shown in Fig. 1. All test specimens were fabricated vertically (along axis Z in Fig. 1) to avoid issues associated with overhanging sections in L-PBF and were randomly distributed in the building platform of the AM machine [3].

The density of the L-PBF CX material was measured in its as-built condition by the Archimedes method using acetone as the immersion medium. The measurements were made three times to ensure the reliability of the results. Then, cross-sectional image analysis was performed on areas of different samples to evaluate the defect distribution in the material. For microstructural analysis, the as-built material was mounted in epoxy resin, ground sequentially with different abrasive pads (up to 2000 grit), and polished with colloidal silica. Subsequently, the polished specimen was etched with Kalling's reagent for 15 s to reveal the microstructural features. Scanning electron microscopy (SEM) was performed using a Hitachi SU3500 scanning electron microscope. The surface roughness (quality) and dimensional accuracy of the fabricated honeycombs were examined using a KEYENCE VR-3200 3D measuring microscope.

Simplified 2D finite element (FE) analysis was used to determine the stress distribution in the honeycomb structures under in-plane external loads in their elastic range. The linear FE models were developed using the FFEPlus solver from Dassault Systèmes, employing triangular

Table 2
Process parameters used for the L-PBF procedure [26].

Power (W)	Scanning speed[a] (mm/s)	Hatch distance (mm)	Layer thickness (mm)	Volumetric energy density (J/mm^3)
260	1000	0.100	0.030	80

[a]Scanning strategy: stripe scanning with 67° interlayer rotations.
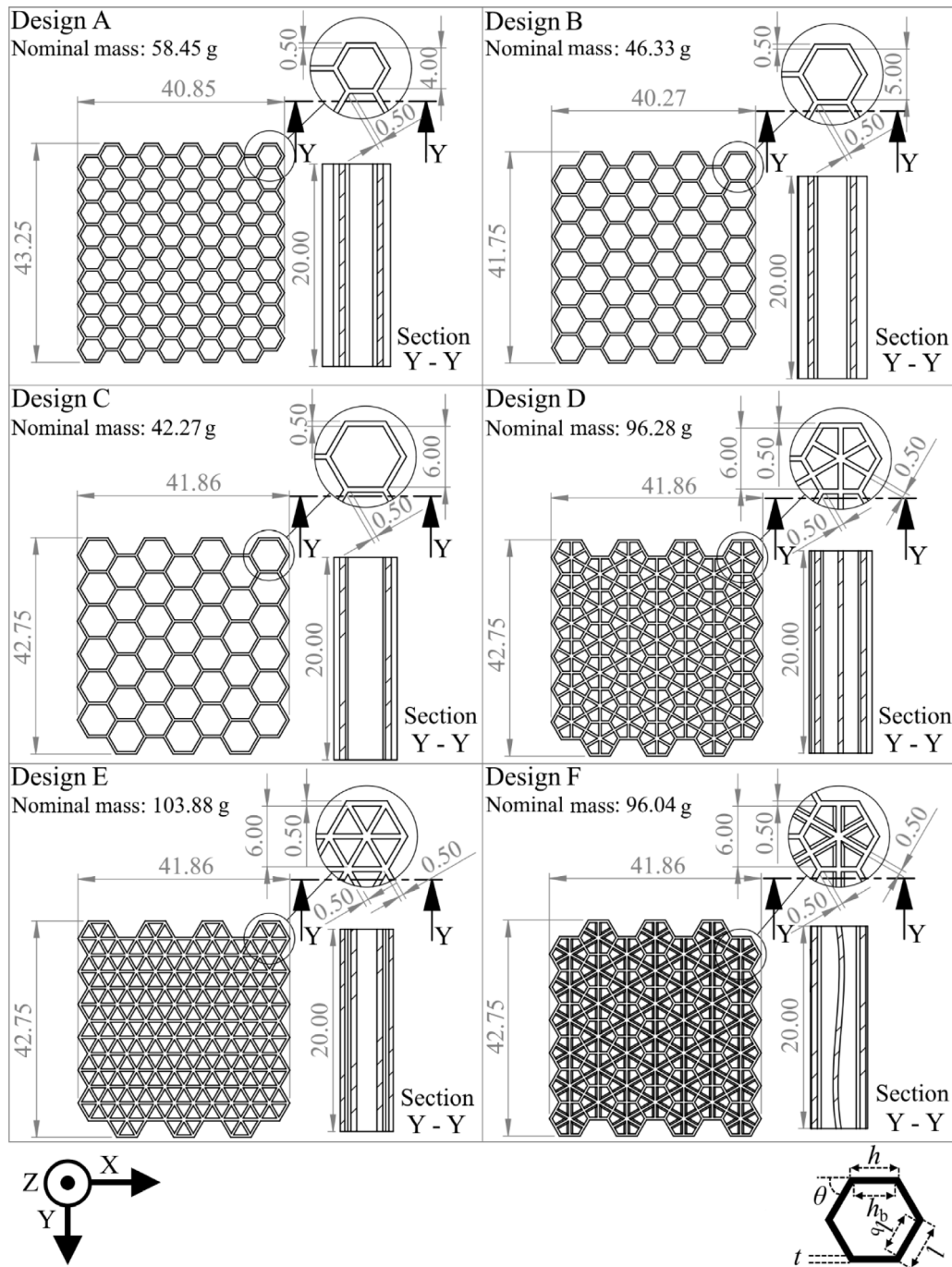
Fig. 1. Honeycomb designs and their characteristics (dimensions in mm).

elements with a mesh size of 0.15 mm. Quasi-static tensile coupon tests were performed using a Galdabini Quasar 600 machine to obtain the required material stress–strain data for input into the FE models. The tensile specimens were manufactured vertically according to ASTM E8 [28], as shown in Fig. 2, and the surface quality was left in the as-built condition. The tensile tests were conducted at room temperature ($\approx$ 20 °C) and with a constant strain rate of 0.001 s^{-1}. An ARAMIS

digital image correlation (DIC) system was used during the tests to record the true stress and logarithmic strain values.

Compression tests were performed to investigate the mechanical performance of the honeycomb structures. First, the specimens were subjected to external quasi-static compressive loading at a constant displacement rate of 0.1 mm/s; the loads were applied in different directions (X, Y, or Z) depending on the type of the tests (in-plane for X
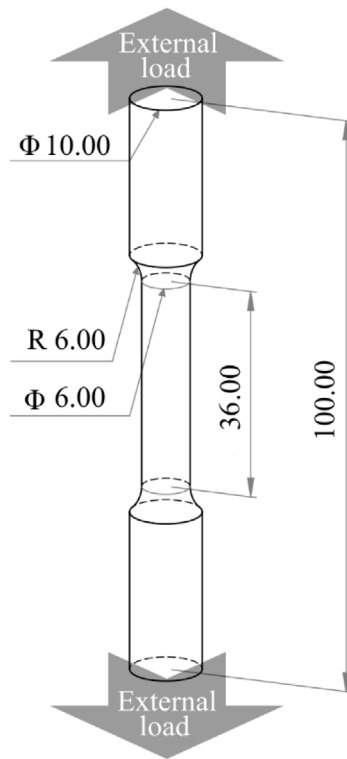
Fig. 2. Schematic view of the tensile specimen (dimensions in mm).

Table 3

Geometrical and structural characteristics of the honeycombs (for a visual representation of the parameters, see Fig. 1).

Design	$h = l$ (mm)	$h_b = l_b$ (mm)	A_{app} [a] (mm²)	A_{eff} [b] (mm²)	ρ_H [c] (g/mm³)
A	2.600	2.310	1627	379.5	1.797×10^{-3}
B	3.180	2.890	1513	300.9	1.530×10^{-3}
C	3.750	3.460	1584	274.5	1.334×10^{-3}
D	3.750	3.460	1584	625.2	3.039×10^{-3}
E	3.750	3.460	1584	674.6	3.279×10^{-3}
F	3.750	3.460	1584	625.2	3.032×10^{-3}

t = 0.5 mm for all designs
$\theta = 60°$ for all designs.
[a] Apparent area: overall cross-sectional area consisting of cell walls and hollow areas between them.
[b] Effective area: actual cross-sectional area consisting of cell walls.
[c] Honeycomb density = (Nominal mass)/(A_{app} × honeycomb height (20 mm in the current study)).

material in its as-built condition, similar to other maraging steels processed by L-PBF, consisted of a combination of martensite with small isolated islands of retained austenite scattered among the martensitic features [30,31]. These microstructural features are shown in Fig. 3(b).

The geometrical and structural characteristics of the honeycombs according to their nominal dimensions are given in Table 3. The frontal views of the fabricated designs and some of the measurements performed to confirm the accuracy of the L-PBF procedure are shown as examples in Fig. 4. The surface qualities of the original designs are shown in Fig. 5. According to the measurements, the average surface roughness (R_a), mean roughness depth (R_z), and dimensional accuracy of the fabricated honeycombs were R_a = 3.0 μm, R_z = 20 μm, and ±30 μm, respectively, regardless of the type of cell design. The results of the tensile tests and mechanical properties of the L-PBF CX material are presented in Fig. 6 and Table 4.

3.1. Compression tests

The manufactured structures were subjected to compressive loads in different directions to evaluate their mechanical performance in different orientations. The compression tests are divided into two groups: out-of-plane (external load in the Z direction) and in-plane (external load in the X or Y direction); these are explained in more detail in the following sections.

3.1.1. Out-of-plane compression tests

The force–displacement data and the results of the out-of-plane tests are shown in Fig. 7 and Table 5, respectively. For the original designs (A, B, and C), the yield force (F_y) and the ultimate force (F_u) increased at initial buckling when the cell size was reduced (hereafter, the loading direction associated with each parameter being denoted by a subscript in parentheses in the abbreviation, e.g., $F_{y(Z)}$ for the yield force under out-of-plane compression). Decreasing the cell size increased both the elastic energy absorbed and the total absorbed energy denoted by $U_{e(Z)}$ and $U_{t(Z)}$ (see Table 5); the energy values are calculated based on the areas beneath the force–displacement diagrams. It is also apparent that the tangent modulus in the Z direction ($E_{e(Z)}$) had an inverse relationship with cell size. Increasing the displacement rate to 1.8 mm/s did not significantly affect the mechanical performance of the printed structures. As for the modified designs, the inner walls improved the performance of the structures in all the aspects listed in Table 5, regardless of the type of reinforcement. However, design E had the highest values of $U_{t(Z)}$, $U_{e(Z)}$, $E_{(Z)}$, $F_{y(Z)}$, and $F_{u(Z)}$ when compared to the others.

3.1.2. In-plane compression tests

The force–displacement data from the in-plane compression tests in the X and Y directions are shown in Figs. 8 and 9, respectively. In
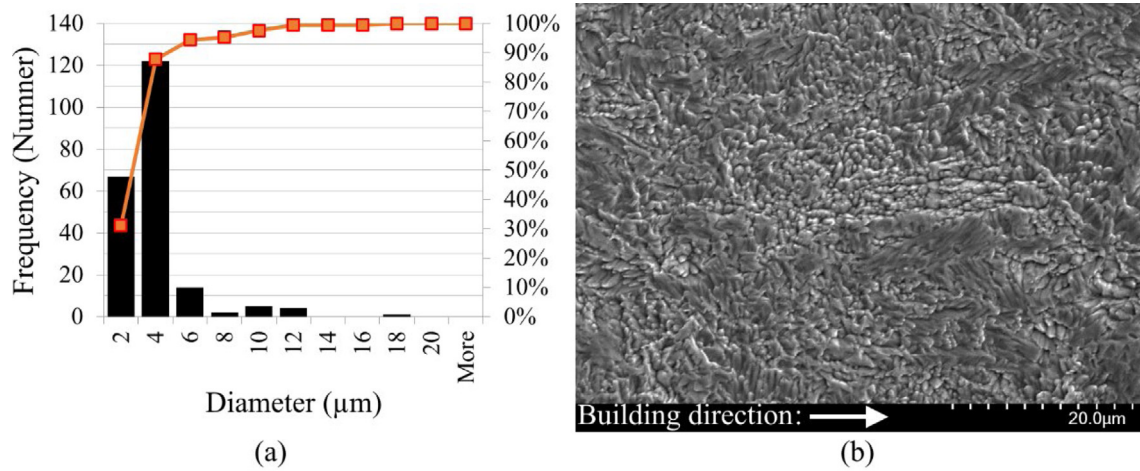
or Y and out-of-plane for Z in Fig. 1). The tests were then repeated at a displacement rate of 1.8 mm/s to study the effects of the loading rate on the mechanical behaviour of the structures. A total of six compression tests, a combination of three directions and two displacement rates, were carried out for each design. The compression tests were stopped at a displacement of 11 mm when loaded in the Z direction and 22 mm when loaded in the X or Y direction, where the honeycombs were compressed to 50% of their original lengths. Beyond this compression limit, significant densifications within the specimens occurred in the current study, similar to [14]. Finally, the ARAMIS system was used to record the deformation progress during the tests.

Drop tests were used to study the response of honeycomb structures to impact loads. The drop mass and drop height for the tests were 45 kg and 3340 mm, respectively. The test was performed for each design by applying the impact load along the Z direction. The test was then repeated for each design by applying the impact load in the X and Y directions (a total of three tests for each design). Finally, the responses of the honeycomb structures to the impact load were compared by their deformations after the impact. A Phantom VEO 710L camera recorded each impact at an average frame rate of 24 000 fps to capture the deformations.

3. Results

Density measurements using the Archimedes method estimated the relative density of the L-PBF CX material to be 99.9% ± 0.1% (≈ 7.7 g/cm³), considering the accuracy of the approach for dense AM metals [27,29]. After the density measurements, areas of 1200 × 700 μm² from two different samples were analysed to evaluate the defect distribution. These areas were selected from the planes parallel to the building direction. The statistical data of the defects are shown in Fig. 3(a). According to the data, more than 80% of the detected defects were spherical and smaller than 5 μm in diameter. The distribution of the defects was relatively uniform, and no signs of clustering were observed in the examined areas. The microstructure of the L-PBF CX

Fig. 3. (a) Defect distribution data and (b) microstructural features of as-built L-PBF CX material.

Table 4
Quasi-static mechanical properties of L-PBF CX material according to the tensile test.

Young's modulus (GPa)	0.2% proof stress (MPa)	Tensile strength (MPa)	Uniform elongation (%)	Elongation (%)
169.0	867.1	1031.8	2.000	13.90

Table 5
Mechanical performance of the honeycombs under out-of-plane compression.

Design	Displacement rate (mm/s)	$U_{t(z)}$ (J)	$U_{e(z)}$ (J)	$E_{e(z)}$ (kN/mm)	$F_{y(z)}$ (kN)	$F_{u(z)}$ (kN)
A	1.000×10^{-1}	4513	126.0	499.0	334.0	469.0
A	18.00×10^{-1}	4424	146.0	497.0	354.0	476.0
B	1.000×10^{-1}	3252	96.00	470.0	283.0	363.0
B	18.00×10^{-1}	3277	97.00	462.0	283.0	368.0
C	1.000×10^{-1}	2746	83.00	413.0	247.0	319.0
C	18.00×10^{-1}	2570	98.00	372.0	255.0	317.0
D	1.000×10^{-1}	8068	310.0	603.0	588.0	807.0
D	18.00×10^{-1}	7615	334.0	594.0	604.0	785.0
E	1.000×10^{-1}	8291	379.0	600.0	649.0	833.0
E	18.00×10^{-1}	8014	363.0	620.0	646.0	833.0
F	1.000×10^{-1}	7804	307.0	594.0	576.0	748.0
F	18.00×10^{-1}	8133	324.0	598.0	600.0	763.0

Table 6
Mechanical performance of the honeycombs under in-plane compression along the X direction.

Design	Displacement rate (mm/s)	$U_{t(x)}$ (J)	$U_{e(x)}$ (J)	$E_{e(x)}$ (kN/mm)	$F_{y(x)}$ (kN)	$F_{u(x)}$ (kN)
A	1.000×10^{-1}	546.0	8.000	33.00	21.00	27.00
A	18.00×10^{-1}	572.0	8.000	35.00	22.00	28.00
B	1.000×10^{-1}	337.0	6.000	18.00	13.00	16.00
B	18.00×10^{-1}	337.0	6.000	18.00	13.00	16.00
C	1.000×10^{-1}	213.0	4.000	11.00	9.000	11.00
C	18.00×10^{-1}	216.0	4.000	11.00	9.000	12.00
D	1.000×10^{-1}	2031	15.00	89.00	48.00	52.00
D	18.00×10^{-1}	2127	18.00	88.00	50.00	54.00
E	1.000×10^{-1}	2513	43.00	134.0	100.0	116.0
E	18.00×10^{-1}	2586	44.00	130.0	101.0	119.0
F	1.000×10^{-1}	2061	15.00	91.00	48.00	53.00
F	18.00×10^{-1}	2068	17.00	84.00	49.00	53.00

addition, the numerical results can be found in Tables 6 and 7. For the original designs, F_y, F_u, U_t, and U_e increased with decreasing cell size, similar to the results of the out-of-plane compression tests. The tangent moduli in the X and Y directions ($E_{(X)}$ and $E_{(Y)}$, respectively) were higher for the structures with smaller cell sizes. Finally, increasing the displacement rate to 1.8 mm/s did not significantly affect the mechanical performance of the structures. Similar to the out-of-plane

results, the internal reinforcements improved the performance under in-plane compression in either the X or Y direction. Design E was superior in all aspects listed in Tables 6 and 7.

3.1.3. Analytical and numerical evaluations

Some parameters related to the mechanical performance of honeycombs made from hexagonal cells can be estimated using equations
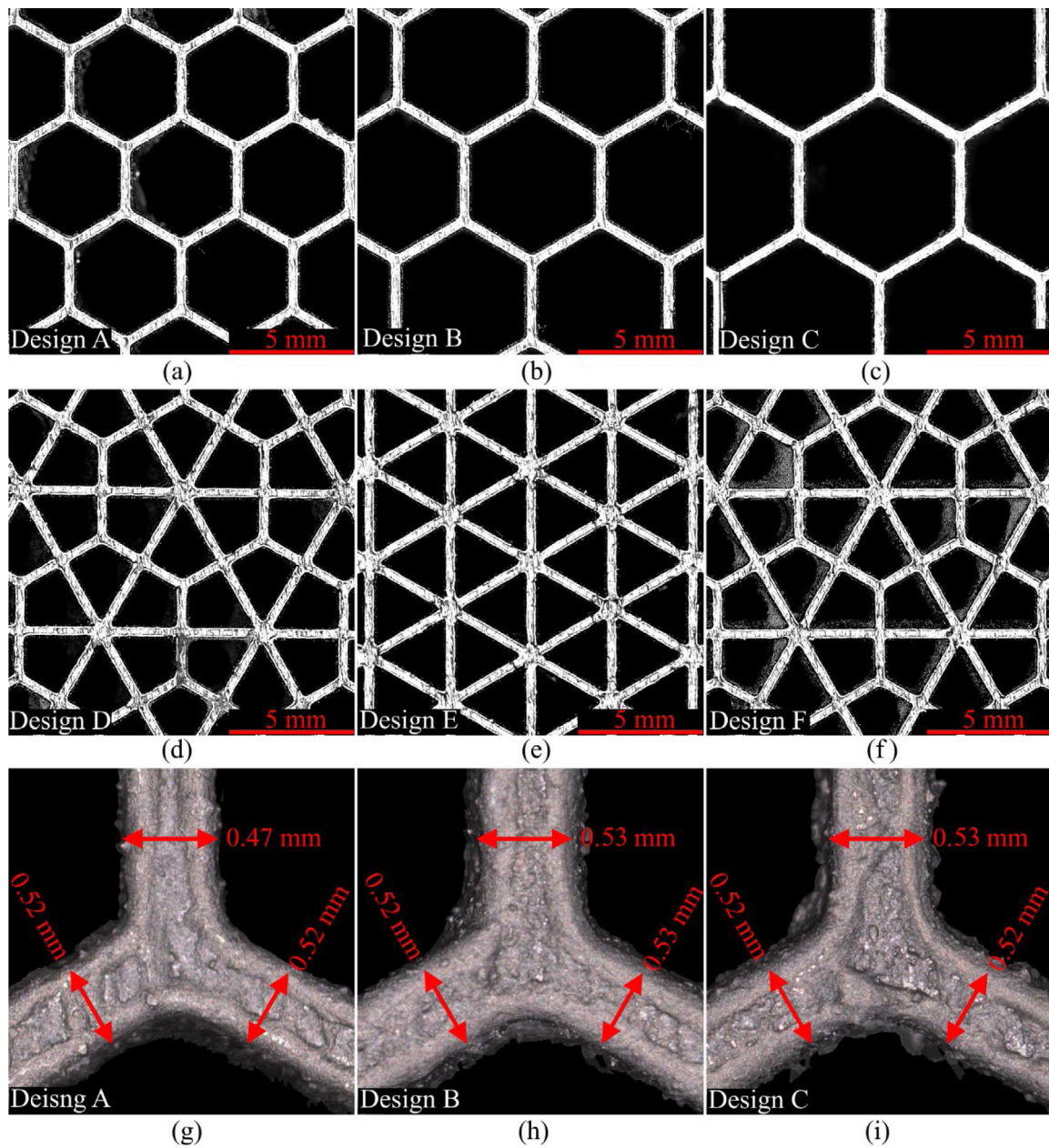
Fig. 4. Frontal views of the fabricated structures (a-f) and examples of dimensional measurements performed to determine the accuracy of the manufacturing process.

Table 7
Mechanical performance of the honeycombs under in-plane compression along the Y direction.

Design	Displacement rate (mm/s)	$U_{t(y)}$ (J)	$U_{e(y)}$ (J)	$E_{e(y)}$ (kN/mm)	$F_{y(y)}$ (kN)	$F_{u(y)}$ (kN)
A	1.000×10^{-1}	488.0	6.000	32.00	18.00	23.00
A	18.00×10^{-1}	474.0	7.000	32.00	19.00	23.00
B	1.000×10^{-1}	298.0	4.000	19.00	12.00	14.00
B	18.00×10^{-1}	292.0	5.000	19.00	12.00	14.00
C	1.000×10^{-1}	199.0	5.000	10.00	9.000	10.00
C	18.00×10^{-1}	212.0	4.000	12.00	9.000	10.00
D	1.000×10^{-1}	2114	27.00	118.0	73.00	83.00
D	18.00×10^{-1}	2127	29.00	117.0	76.00	85.00
E	1.000×10^{-1}	2865	36.00	136.0	91.00	93.00
E	18.00×10^{-1}	2824	36.00	139.0	91.00	94.00
F	1.000×10^{-1}	2078	26.00	117.0	71.00	82.00
F	18.00×10^{-1}	2123	30.00	116.0	76.00	84.00

proposed in the literature for conventionally fabricated cellular structures. Consequently, these equations can also be used for honeycombs fabricated using AM to evaluate how these structures perform under external loads compared to their conventionally manufactured counterparts. For example, Eqs. (1) and (2) can be used to estimate the force required for initial buckling to be triggered under out-of-plane
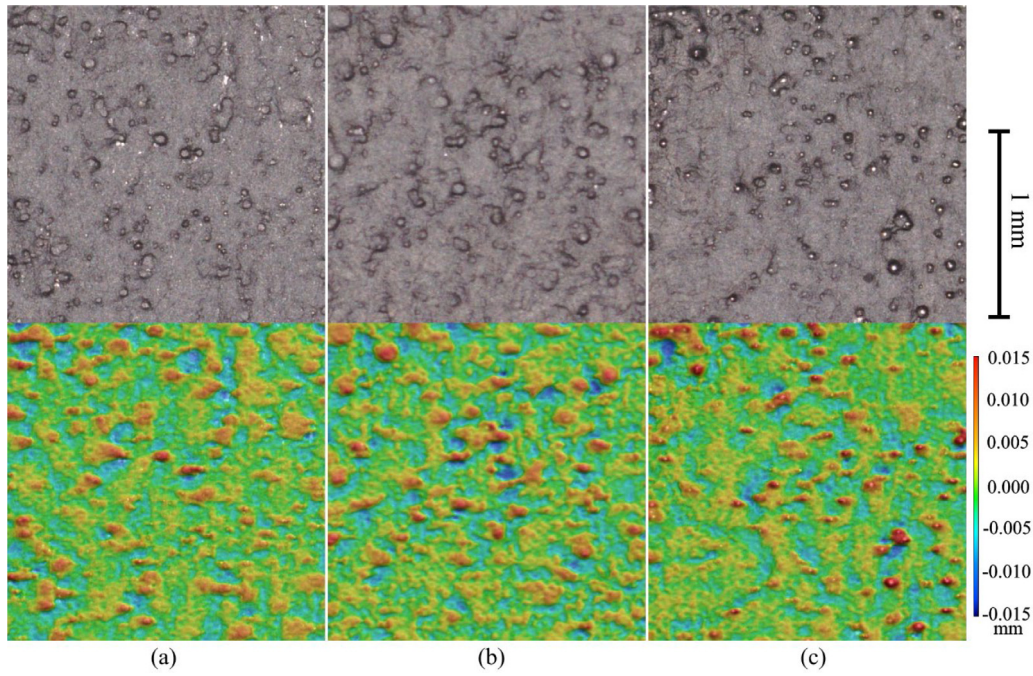
Fig. 5. Surface quality of the original designs: (a) design A, (b) design B, and (c) design C.
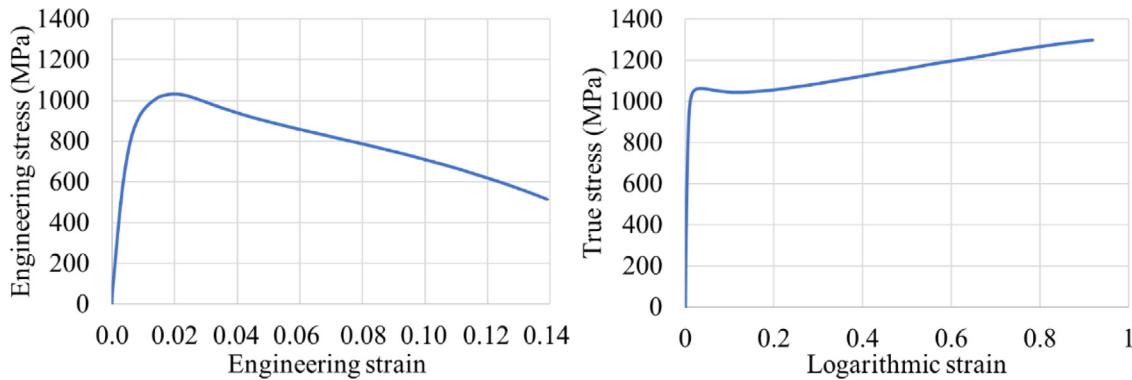

Fig. 6. Engineering stress–strain (left) and true stress–logarithmic strain (right) curves of L-PBF CX.

compression. In addition, Eq. (3) estimates the stress in the cell walls [15,18]:

$$\sigma_{pl(z)} = \sigma_{yield} \times 5.6 \times (t/l)^{(5/3)} \tag{1}$$

$$F_{u(z)} = \sigma_{pl(z)} \times A_{(app)} \tag{2}$$

$$\sigma_{wall} = \sigma_{fw} \times \rho_S / \rho_H, \tag{3}$$

where $\sigma_{pl(z)}$ is the out-of-plane stress required for collapse due to plastic buckling of the hexagonal honeycombs, σ_{yield} is the yield strength of the material, σ_{wall} is the stress applied to the individual cell walls, and σ_{fw} is the flatwise compressive stress, which can be calculated by dividing the applied load by $A_{(app)}$ [15,18].

Regarding in-plane compression, the behaviour of honeycombs can be evaluated using the equation proposed by Gibson et al. [17] (Eq. (4)) to predict the plastic collapse of honeycombs made from hexagonal cells:

$$\sigma_{pl(x)} = \sigma_{pl(y)} = \sigma_{yield} \times (t^2/l^2) \times 2/3, \tag{4}$$

where $\sigma_{pl(x)}$ and $\sigma_{pl(y)}$ are the out-of-plane stress values required for the plastic collapse of the honeycombs in the X and Y directions, respectively. The force values in each direction can also be calculated

by considering the applied load at the onset of the plastic collapse as the multiplication of the stress by the apparent lateral area of the honeycombs. The values that were calculated using Eqs. (1), (2), and (4) are shown in Fig. 10, along with the experimental results for comparison. It should be noted that the equations can only be used for the original designs in this study, as they are only applicable to honeycombs with hexagonal cells without any reinforcements.

In Eq. (4), Gibson et al. [17] considered the behaviour of honeycombs with hexagonal cells under in-plane compressions that are isotropic ($\sigma_{pl(x)} = \sigma_{pl(y)}$), while the experimental results of the current study (Section 3.1.2) and the literature show some minor differences in the behaviour of honeycombs in the X and Y directions [13,16,17]. Therefore, the stress distributions in the honeycombs were analysed via FE to investigate the cause of this anisotropic behaviour. As shown in Fig. 11(a) and (a′), compressive loads applied along the Y direction in the original designs can cause slightly higher stress concentrations at the cell corners than external loads applied in the X direction. Consequently, the values of $\sigma_{u(X)}$ and $F_{u(X)}$ in the original designs were to some extent higher than $\sigma_{u(Y)}$ and $F_{u(Y)}$, respectively. Finally, Fig. 11 also shows the stress distributions of the modified designs for comparison with those of the original designs (the results of design F are not included in the figure because this design had similar results to design D).
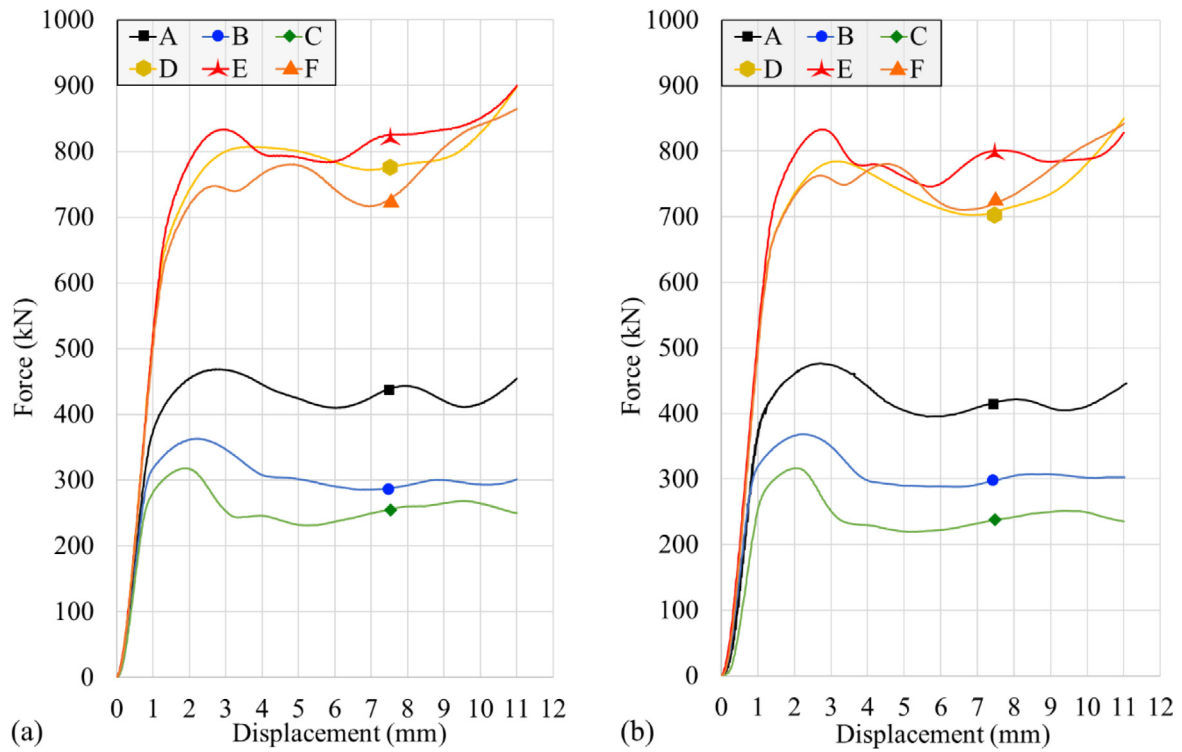
Fig. 7. Force–displacement curves of the honeycombs subjected to out-of-plane compressive loading with a displacement rate of (a) 0.1 mm/s and (b) 1.8 mm/s.
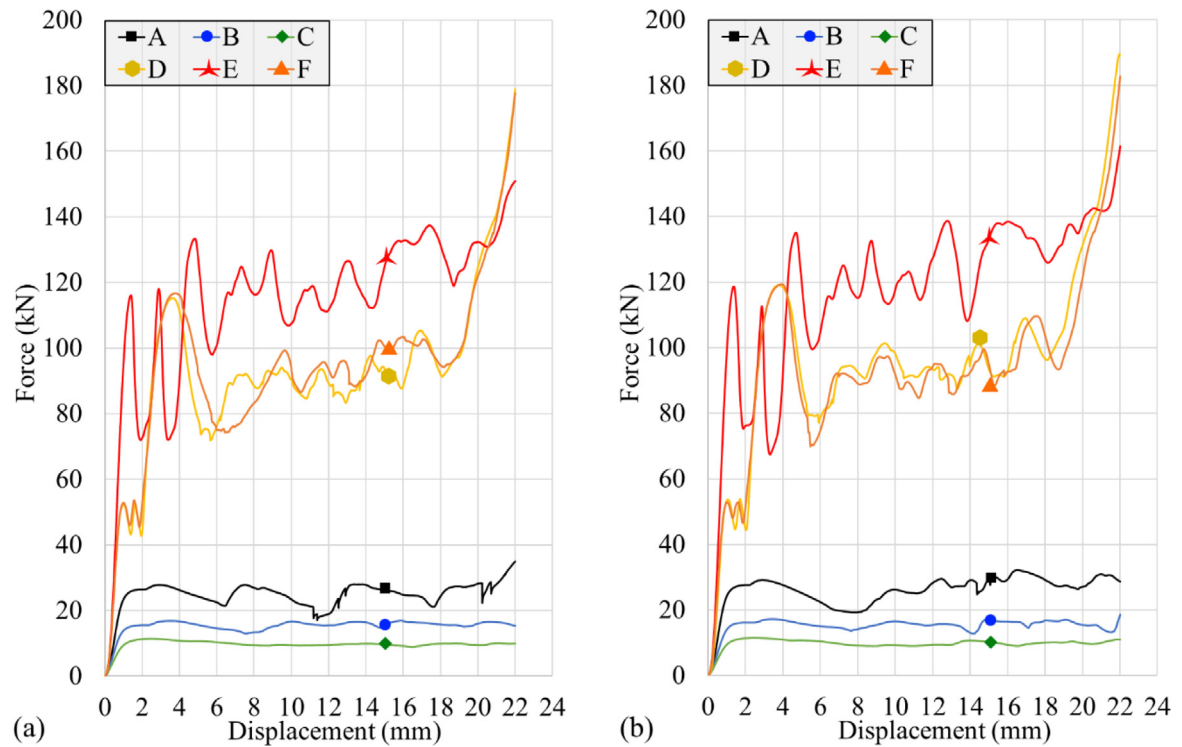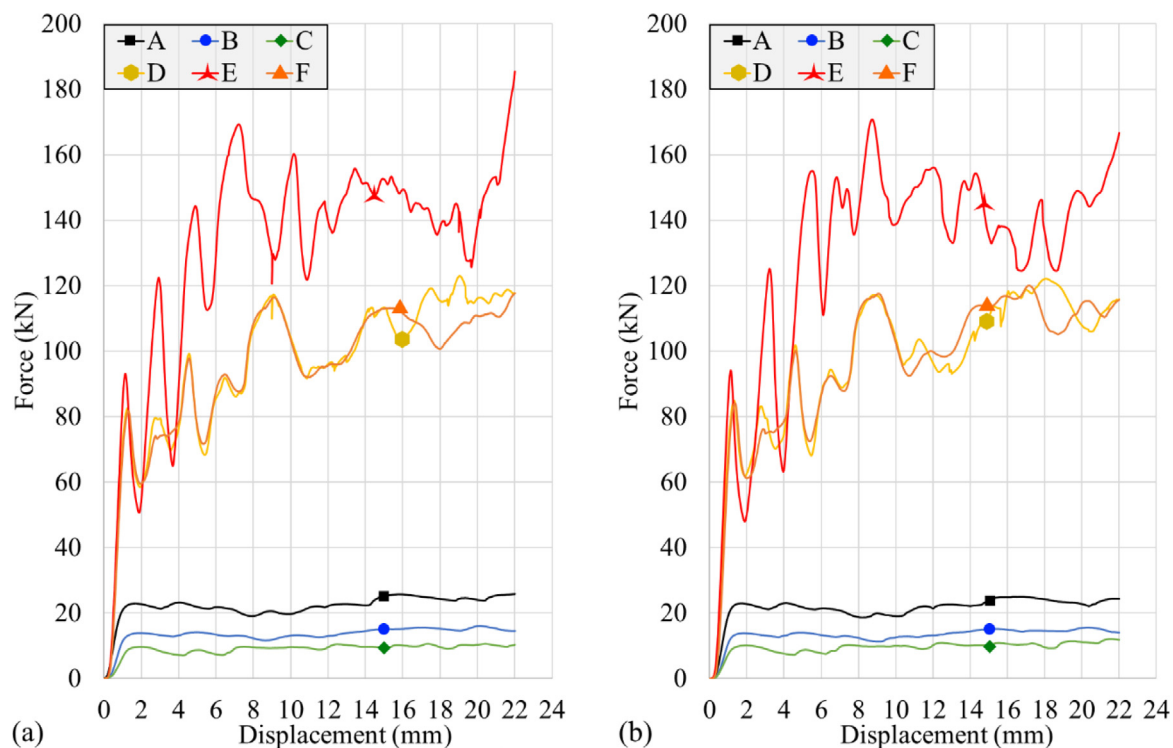

Fig. 8. Force–displacement curves of the honeycombs subjected to in-plane compressive loading in the X direction with a displacement rate of (a) 0.1 mm/s and (b) 1.8 mm/s.

3.2. Drop tests

The results of the drop tests are summarised in Table 8. To compare the resistance of the designs to impact loads, their deformations due to the drop weight are reported in this study. According to the results, the resistance in the Z direction was increased by reducing the cell size in the original designs. However, it was not possible to make the same comparison along the X or Y directions because all original designs were completely deformed after the drop test, as shown for design C in Fig. 12(a) as an example. All modified designs exhibited lower deformations after impact than the original designs. The deformation values of the modified designs did not differ significantly in the Z direction; however, design E with the triangular cells had the best resistance to deformations caused by impact loads in the X and Y directions. Design

Fig. 9. Force–displacement curves of the honeycombs subjected to in-plane compressive loading in the Y direction with a displacement rate of (a) 0.1 mm/s and (b) 1.8 mm/s.

Table 8
Displacements caused by the impact force in the drop test.

Design	A	B	C	D	E	F
Displacement from the impact along Z (mm)	−2.500	−3.800	−4.800	−1.300	−1.300	−1.300
Displacement from the impact along X (mm)	Fully deformed	Fully deformed	Fully deformed	−16.50	−12.40	−15.10
Displacement from the impact along Y (mm)	Fully deformed	Fully deformed	Fully deformed	−15.10	−11.55	−12.75

F exhibited lower deformations in the X and Y directions than design E. The modified designs had anisotropic behaviour under the impact loads in the X and Y directions, as the resulting deformations were different in Table 8. This anisotropy could also have been present in the original designs; however, it was not possible to investigate this phenomenon in the original designs since they were fully deformed by the impact, and the impact load values could not be recorded due to limitations of the testing machine.

4. Discussion

L-PBF CX, as a maraging steel processed by additive manufacturing, is expected to have a martensitic microstructure in its as-built condition. The 99.9% relative density of the processed metal, the uniform distribution of defects, and having the majority of defects smaller than 5 μm in diameter point to the optimum AM parameters being used in this study. According to the literature, porosities in this size range are considered inherent to L-PBF due to gas entrapments originating from the manufacturing process and raw powder. These isolated porosities cannot deteriorate the mechanical properties of AM metals as long as, in most cases, the relative density of the processed metals is above 99%, and no porosity clusters are present in the material [7,32]. Furthermore, the surface quality of the manufactured honeycombs was within the range of optimal values specified in the material data sheet (Ra ≤ 5 μm for vertical surfaces) [27].

The fabricated structures did not show significant dimensional inaccuracies that can be considered to be severe geometrical distortions in the finished parts (maximum value of ±30 μm for 500 μm wall thickness). It should be noted that it was not possible to measure the wall thickness with satisfactory accuracy because the unmelted powder particles stuck to the walls (see Fig. 4(g–i)). The ferromagnetic nature of the material exacerbated this problem. This measurement issue associated with L-PBF honeycombs has also been addressed in similar studies in the literature [3]. Consequently, the maximum thresholds of the measured dimensions were considered for the calculation of dimensional tolerances to account for the worst case. The powder particles attached to the honeycombs were not expected to alter their load-carrying capacity significantly since the particles were relatively small compared to the wall thickness, and the bonds between the particles and their substrate were expected to be weak [15]. Although studies such as [10] have reported better geometrical qualities for honeycombs with relatively larger cells due to their relatively better heat dissipation during AM, such inconsistency in dimensional accuracy and surface quality was not observed in the cell size range considered in the current study.

4.1. Mechanical tests

Similar to conventionally manufactured honeycombs [15], the load–displacement curves of the L-PBF honeycombs in the current study can be divided into five distinct regions for both the out-of-plane and in-plane compression cases. These regions are indicated by arrows and labels for design C in Fig. 13. Regarding out-of-plane compression, all the honeycombs failed by cell wall buckling at the bottom of the structures. As an example, Fig. 13 shows the failure sequence for design C under out-of-plane compression. The remainder of the specimens failed in a similar manner until they reached their densification threshold and began to behave like a solid material (where a substantial increase in
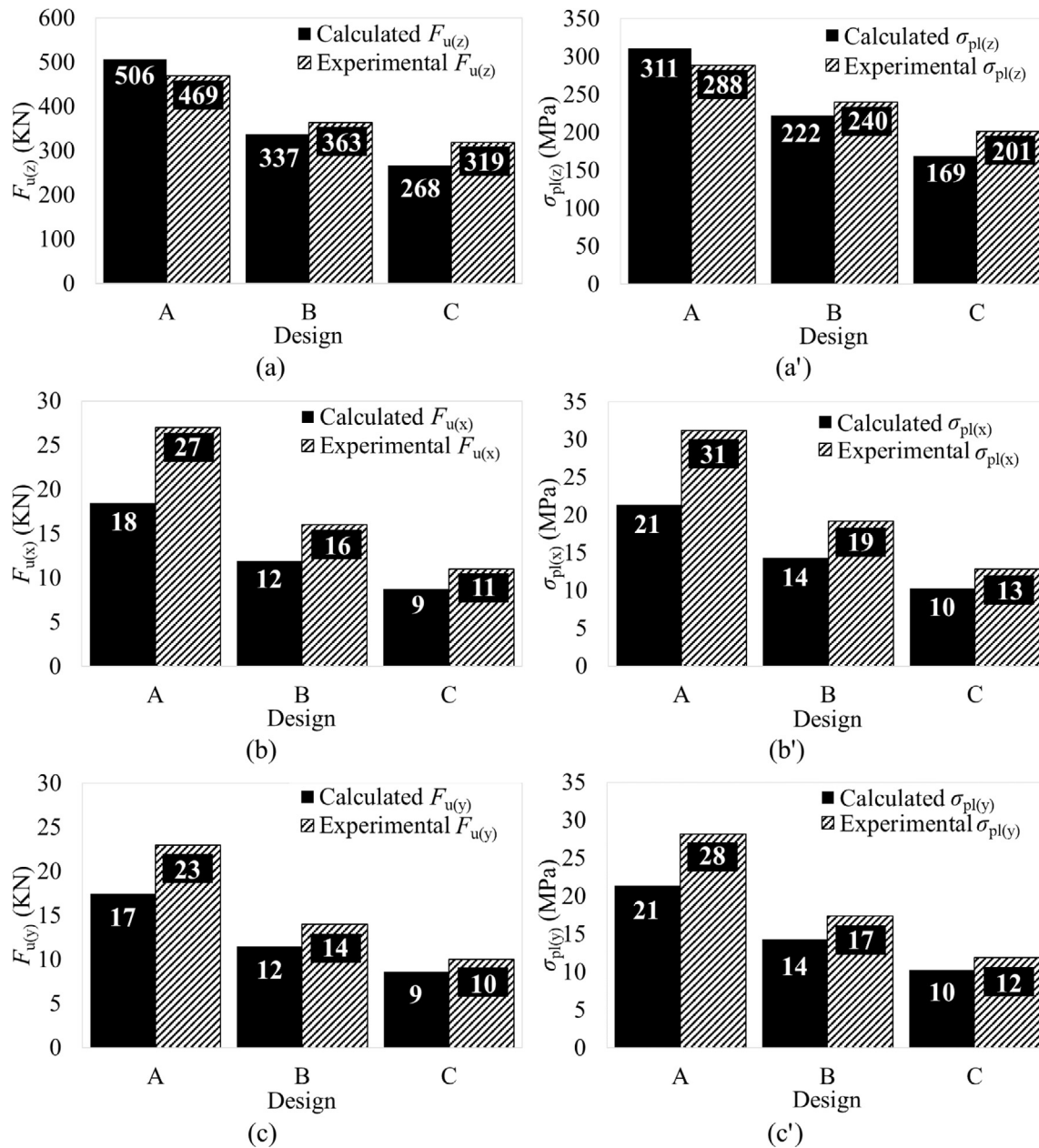
Fig. 10. Analytical calculations and their comparisons with the experimental results from the compression tests with a displacement rate of 0.1 mm/s.

compression load would be required for further deformation). Stress values in the cell walls of the original designs were calculated using Eq. (3), and their values were 1235 MPa, 1207 MPa, and 1162 MPa for designs A, B, and C, respectively. Therefore, failure in the original designs involved significant plasticity within the cell walls since all the calculated values were higher than the elastic limit of the L-PBF CX material [15].

Failure of the honeycombs under in-plane compression initiated in the cell corners, regardless of the design type, as shown in Figs. 14–19. The failure initiation sites in these figures are in agreement with the stress concentration points shown in Fig. 11. It can be concluded that under in-plane compression loads, failure initiated in the corners with the highest stress concentrations. The majority of the failure sequence was then driven by shearing of the cell walls. The 45° angle between the failure sequence and the loading direction in the figures also indicates the shearing mechanism. However, this mechanism was less pronounced in design E when it was loaded in the Y direction. There is a sharp drop in load after each failure in all the tests, indicating

the presence of low stresses throughout the structure owing to the rearrangement of the remaining cells. After each load drop, the load begins to increase again as the subsequent array of cells, after the rearrangement, begins to deform and resist the applied load. This process repeats until all rows of cells collapse and honeycomb densification initiates [16]. This kind of cellular collapse with successive peaks and troughs in the load versus deformation relationship, often termed cellular buckling [33] or snaking [34], is familiar from a number of different problems where highly unstable buckling is followed sequentially by restabilisation. Such behaviour has also been observed during the buckling of cylindrical shells [35], during kink-banding of laterally confined layers under longitudinal compression [36], and in the interactive buckling of thin-walled structures [37–39].

For hexagonal honeycombs, the tangent modulus depends on the material properties and the frictional force between the specimen and the grips of the compression test rig [10]. By decreasing the cell size in the original designs, the contact area and friction between the specimens and the grips became more prominent, and the tangent
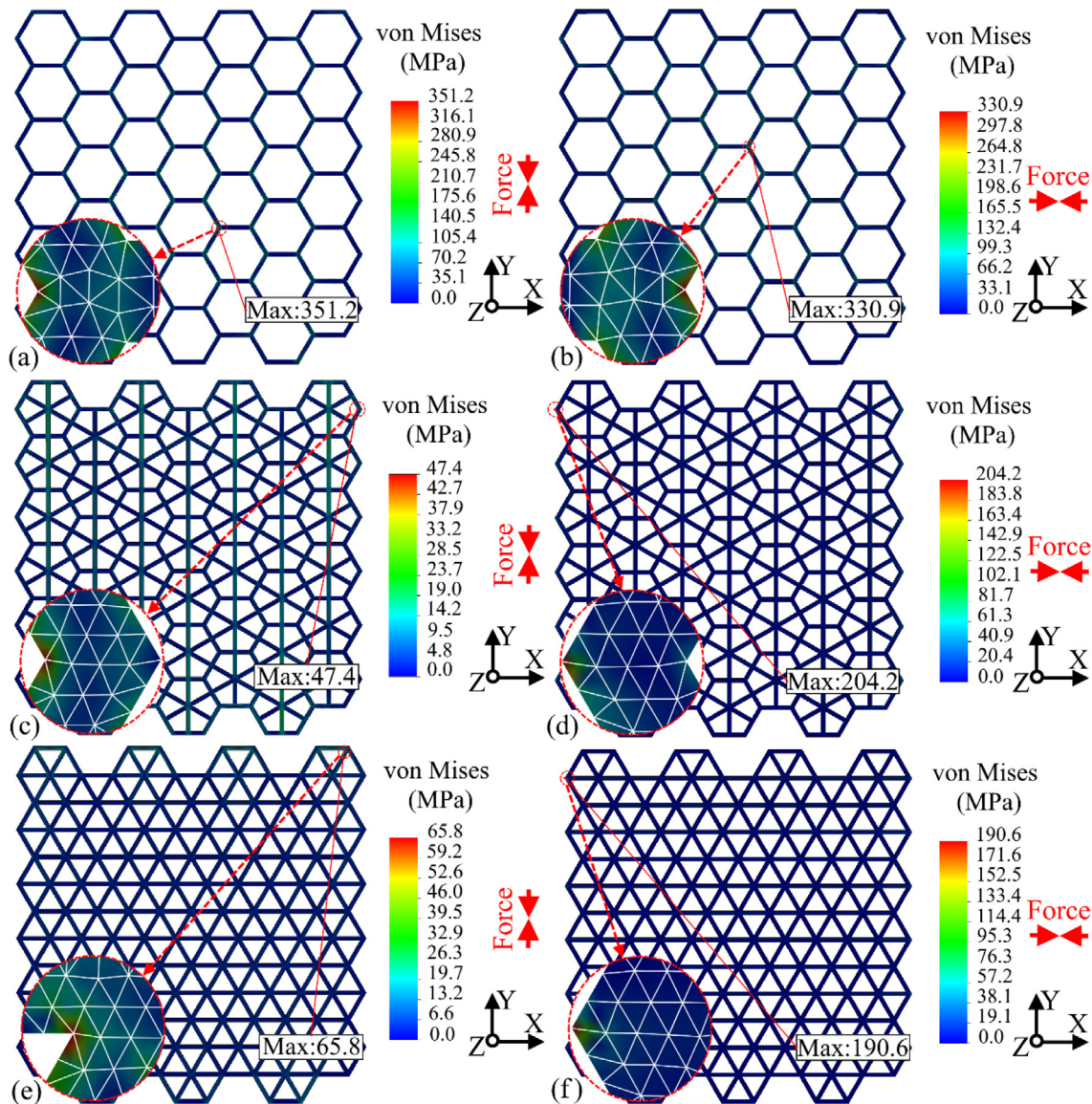
Fig. 11. FE analysis of the elastic equivalent stresses for different designs under a compressive load of 1000 *N* applied in the Y (a, b, and c) or X (a′, b′, and c′) direction: (a, a′) design C, (b, b′) design D, and (c, c′) design E.

modulus increased, as shown in Fig. 20. In addition, the number of peaks and troughs of the load during the test depends on the cell size for in-plane compression, as seen in Figs. 8 and 9, where smaller cells resulted in more frequent increases and reductions since they provided the honeycombs with more cells for rearrangement after each cell failure and subsequent load drop. A long and stable deformation plateau is desirable for crashworthy structures since the effectively small structural stiffness in this phase reduces stress propagation; and, a high number of peaks and troughs is attributed to a more brittle failure mechanism in hollow structures, e.g., honeycombs [14]. However, presently, although structures with smaller cells exhibited less stable plateaus with more load peaks and troughs, they absorbed significantly more energy prior to their densification (design C compared to A, for example).

Finally, structures with smaller unit cells and higher ρ_H values required higher deformation loads in their compression tests and therefore absorbed a higher total energy. This behaviour is similar to that of conventional honeycombs [10]. By comparing the changing pattern in the values presented in Fig. 20(a–c) with the density values in Fig. 20(d), it can be concluded that ρ_H was the main parameter determining the behaviour of the honeycombs under compressive loads.

According to the literature, specific values of the total energy absorbed or ultimate force are better parameters to compare the crashworthiness of honeycombs. These specific values can be calculated based on the relative density or the weight of honeycombs [2,3], as presented in Fig. 21.

According to Fig. 21, the crashworthiness of designs D and F in the Z direction are found to be slightly better than design E when considering the specific total energy absorbed, although all the mechanical properties of design E are superior to those of the other designs (Fig. 20). By considering the specific ultimate force as the basis for the comparison, designs A and D show slightly better results than design E in the Z direction. The slightly inferior performance of the triangular honeycombs under out-of-plane loads was predicted via FE modelling by Shah & Kapania in [9], but no experiment was conducted in that study to confirm their FE results. However, it should also be noted that design E had superior impact resistance in all directions compared to the other designs. Therefore, the overall results for design E in the current study are very promising, to the extent that whenever a honeycomb structure with acceptable performance along its major axes and under a wide range of load scenarios, from quasi-static to dynamic, is required, design E with triangular cells appears to be the best option.
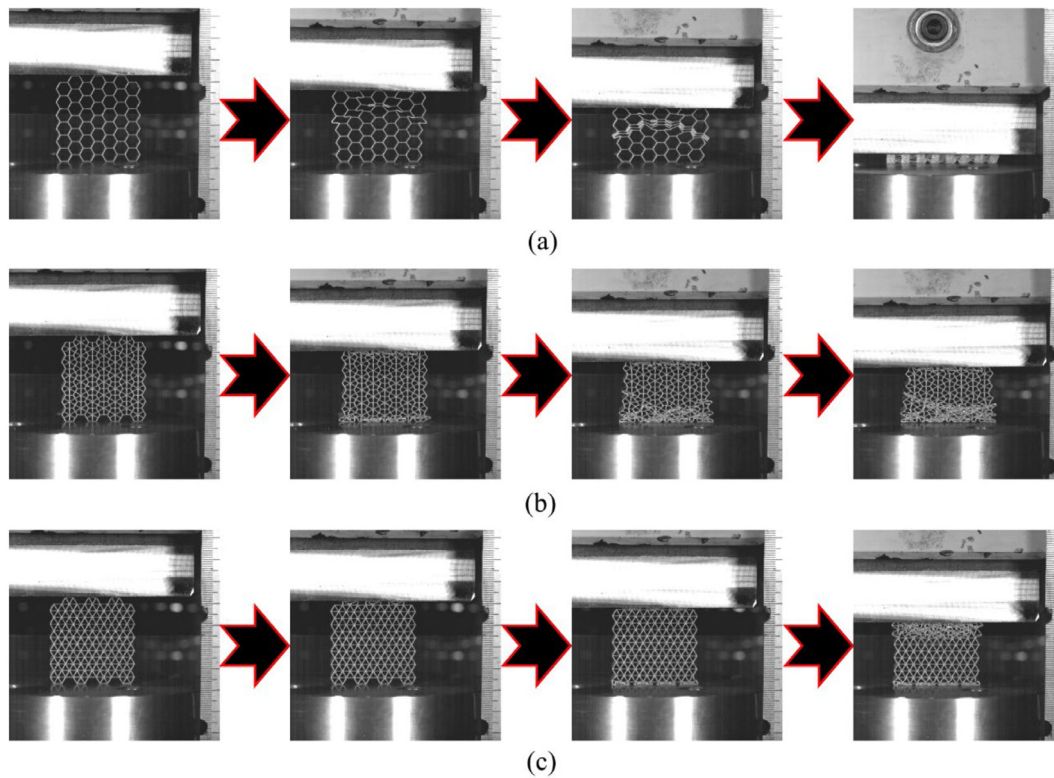
Fig. 12. Drop test progress for different samples from the beginning of the impact until its end: (a) design C, (b) design D, and (c) design E. The impact load was applied along the Y direction (with reference to Fig. 1) in all the images.
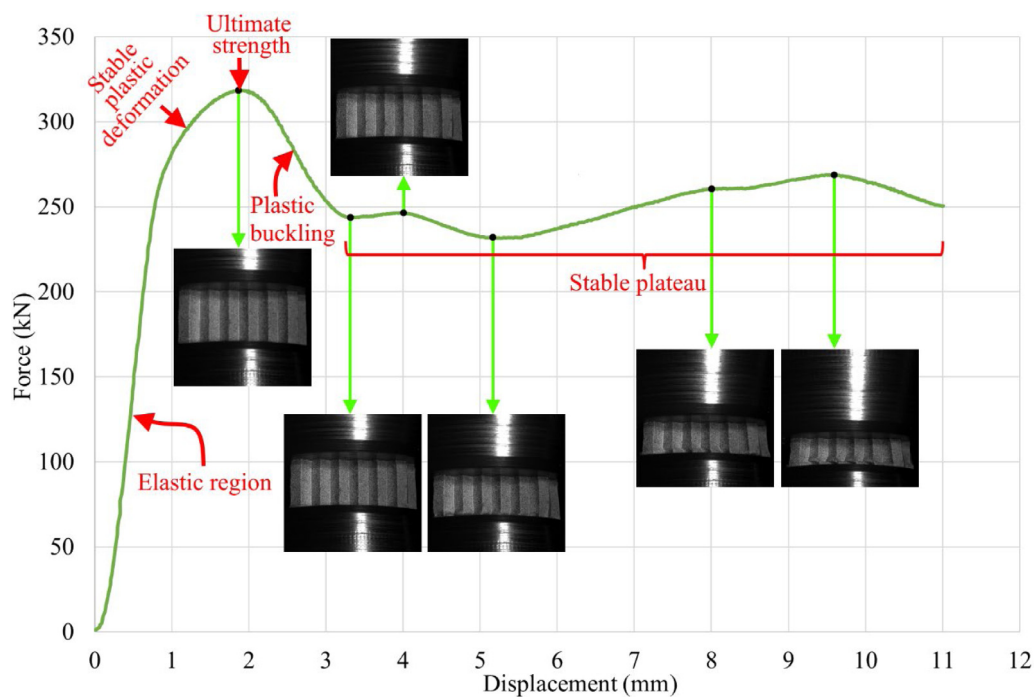

Fig. 13. Deformation sequence for of design C compressed in the Z direction.

The results of the drop tests showed a similar trend to those of the compression tests. Consequently, it can be concluded that ρ_H is the primary factor determining the structural performance under quasi-static or dynamic loads. However, considering the resultant displacement as the comparison criteria, design F had better performance under impact load when compared to design D. Therefore, it made the design more resistant to deformations under impact loads, although adding a gentle longitudinal curvature to the internal walls did not significantly affect
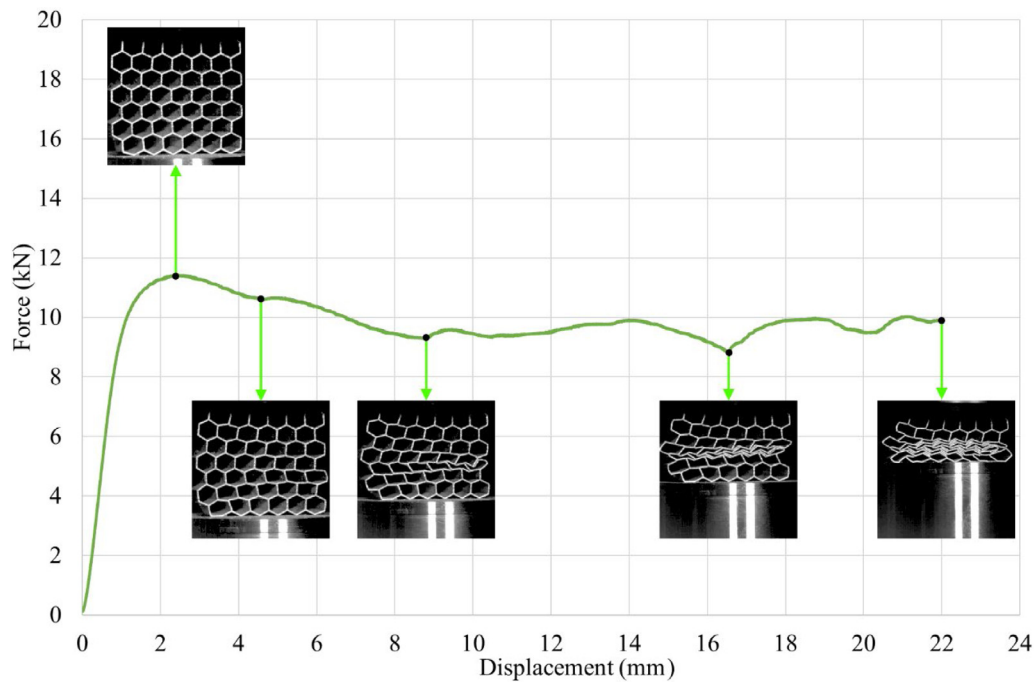
Fig. 14. Deformation sequences for design C compressed in the X direction.
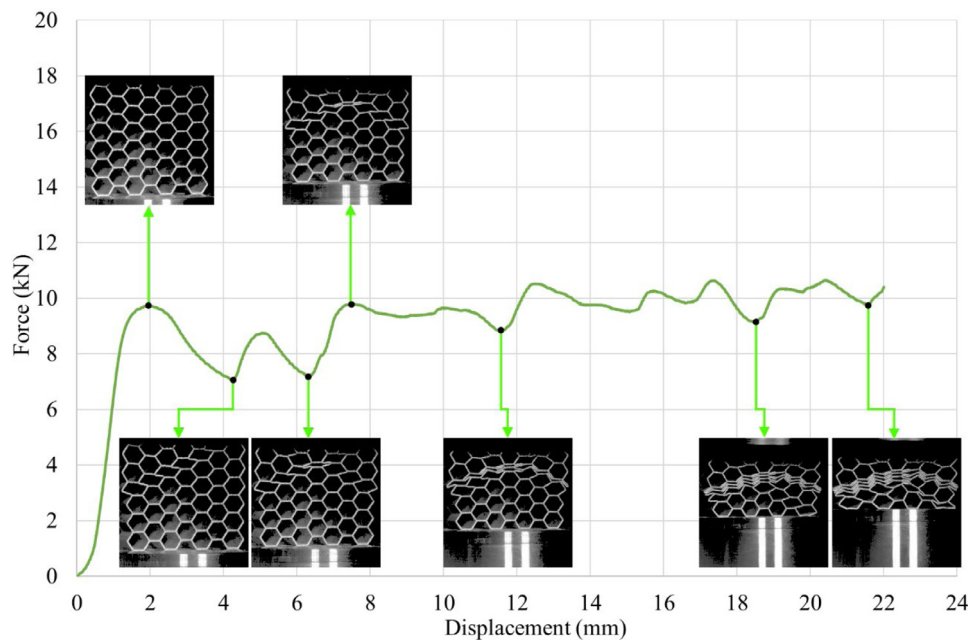
Fig. 15. Deformation procedure of design C compressed in the Y direction.

the performance of the modified design under quasi-static load. In conclusion, such a design modification can facilitate the structure in resisting the inertia force imposed by the dynamic loading condition.

Finally, the similar performance of the structures under the displacement rates of 0.1 mm/s and 1.8 mm/s can be attributed to the insensitivity of the L-PBF CX material to the effects of changes in strain rate, which stems from its martensitic microstructure and the lack of strain-induced microstructural transformations. However, this issue requires further investigation for clarification and should be considered in future research.

5. Conclusions

This study investigated the mechanical properties and crashworthiness of six different honeycomb designs manufactured by the L-PBF technique. The results were used to evaluate the suitability of additive manufacturing, as a novel alternative method, for fabricating honeycomb structures. The following conclusions have been drawn from the current study:

- Owing to the high relative density of the material processed by L-PBF, lack of critical defects, and acceptable mechanical properties
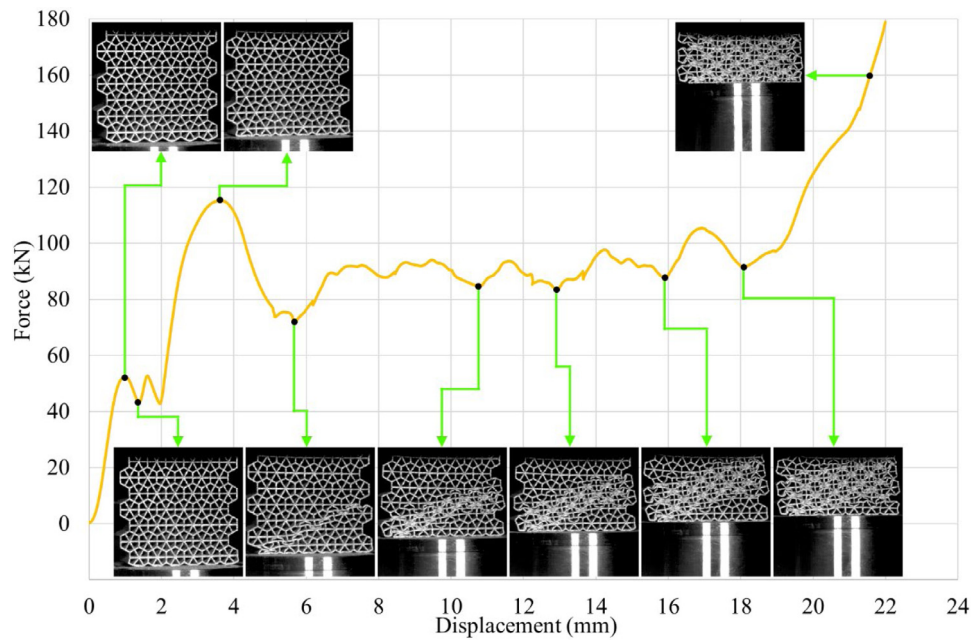
Fig. 16. Deformation sequences for design D compressed in the X direction.
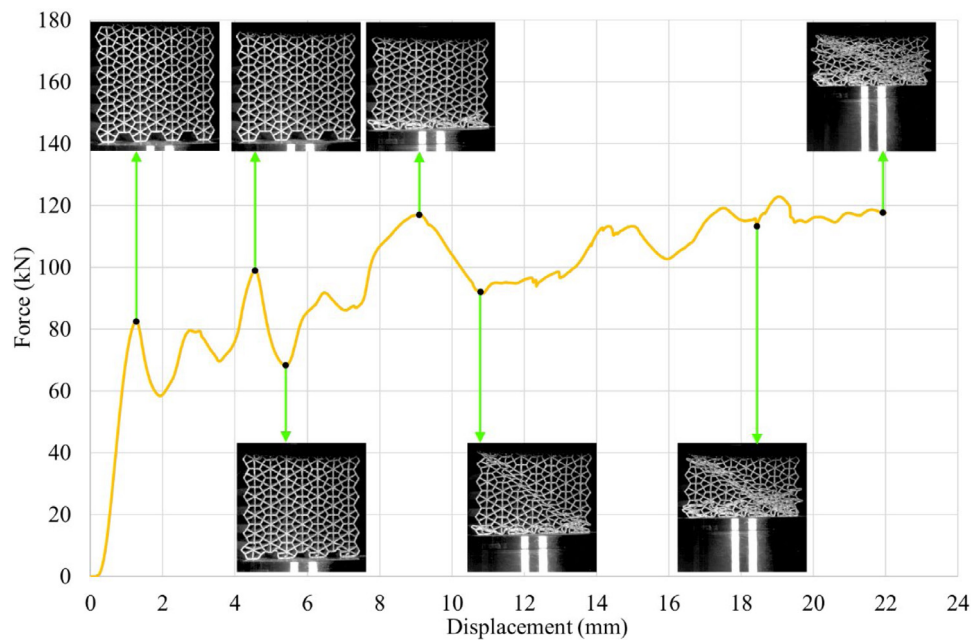

Fig. 17. Deformation procedure of design D compressed in the Y direction.

in the as-built condition, L-PBF can be considered to be a viable option for manufacturing honeycomb structures. In addition, relatively acceptable dimensional accuracy and geometrical quality that has been presently observed in L-PBF honeycombs reinforce this claim.

- Structural failure was initiated by material plasticity along the cell walls in the out-of-plane compression, while the failure was initiated at the stress concentration points located at the cell corners under the in-plane loading.
- Design modifications by DfAM significantly improved the performance of the honeycombs in general. However, additional curvature to increase the rigidity of the internal walls in the

modified designs did not affect the behaviour of the honeycombs under quasi-static loads, while there was a significant decrease in the displacement caused by dynamic impact loads (i.e., improved performance).

- Relative density appeared to be the most important factor influencing the behaviour of the honeycombs in the mechanical tests. Consequently, hexagonal honeycombs (original designs) with relatively smaller cells showed better performances under various mechanical loads.
- Regarding the influence of cell design, considering the original and modified designs altogether, honeycombs with triangular
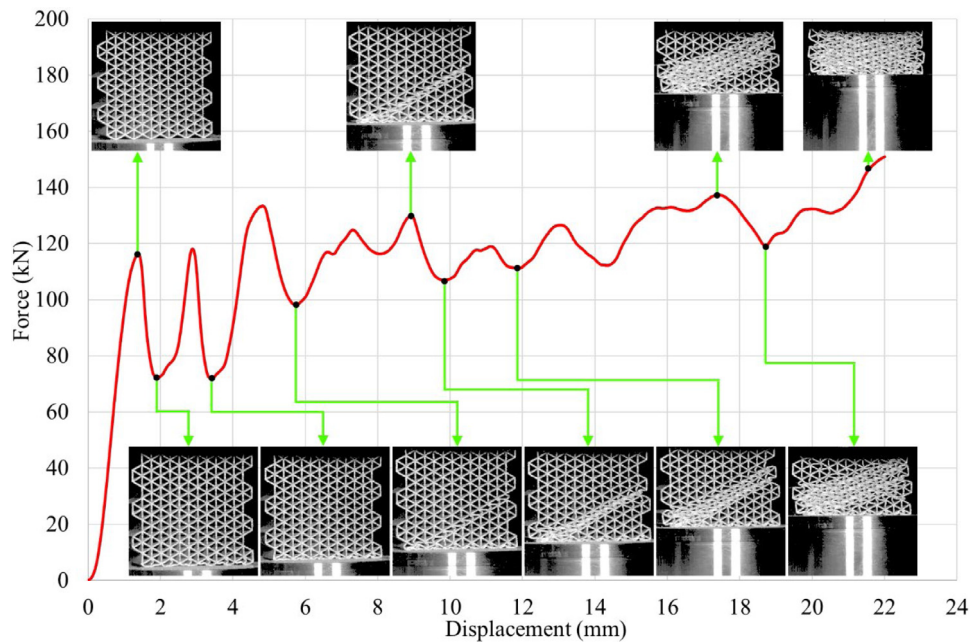
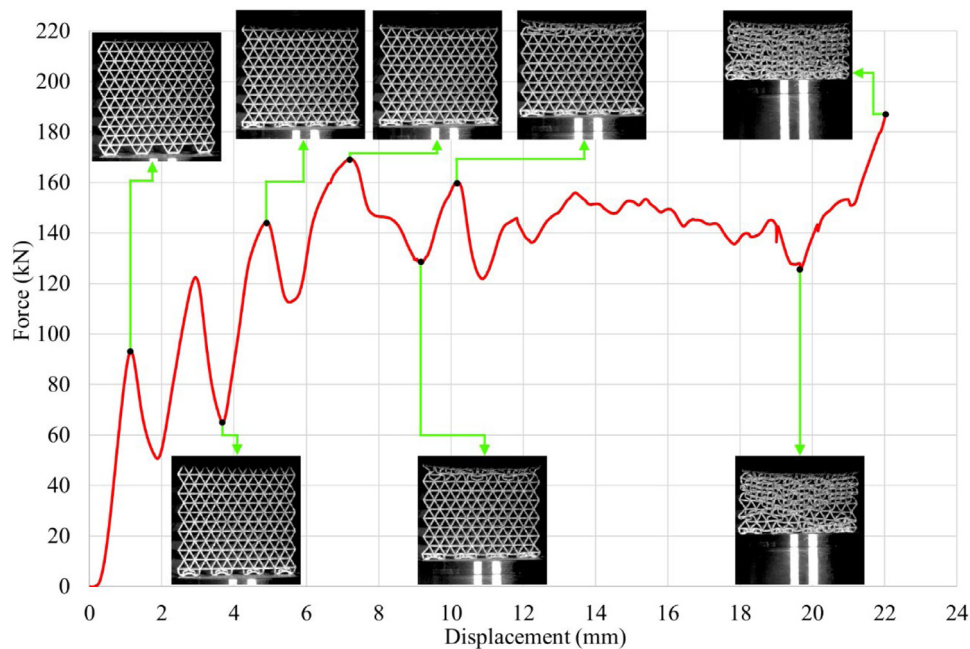**Fig. 18.** Deformation sequences for design E compressed in the X direction.

Fig. 19. Deformation sequences for design E compressed in the Y direction.

cells outperformed their counterparts with hexagonal or diamond-shaped cells in overall comparisons dealing with loading scenarios applied along different directions and under strain rates varying from quasi-static to impact compression.

- Analytical equations used to calculate ultimate force and out-of-plane stress required for collapse due to plastic buckling underestimated the experimental results for the L-PBF honeycombs, except for the case of design A under out-of-plane loads. Consequently, these equations, which were developed for conventionally manufactured honeycombs, seem applicable without safety concerns for L-PBF honeycombs under in-plane loads. Regarding the honeycombs loaded out-of-plane, using the equations for honeycombs with low relative densities, e.g., design A in the

current study, might raise some safety concerns due to the slight overestimations shown in Fig. 10(a, b). However, applying a safety factor for such calculations might overcome such issues. But such a factor would need to be calibrated in future work.

Finally, honeycombs, hollow structures, and lattice structures produced by additive manufacturing still require further investigation. Finite element analysis (FEA) can be considered to be a powerful tool for evaluating the performance of these structures under various loading scenarios. Consequently, a more sophisticated FEA of the original and modified honeycombs used in the current study is projected in future research to evaluate the behaviour of the honeycombs beyond their elastic limit and to ultimate collapse.
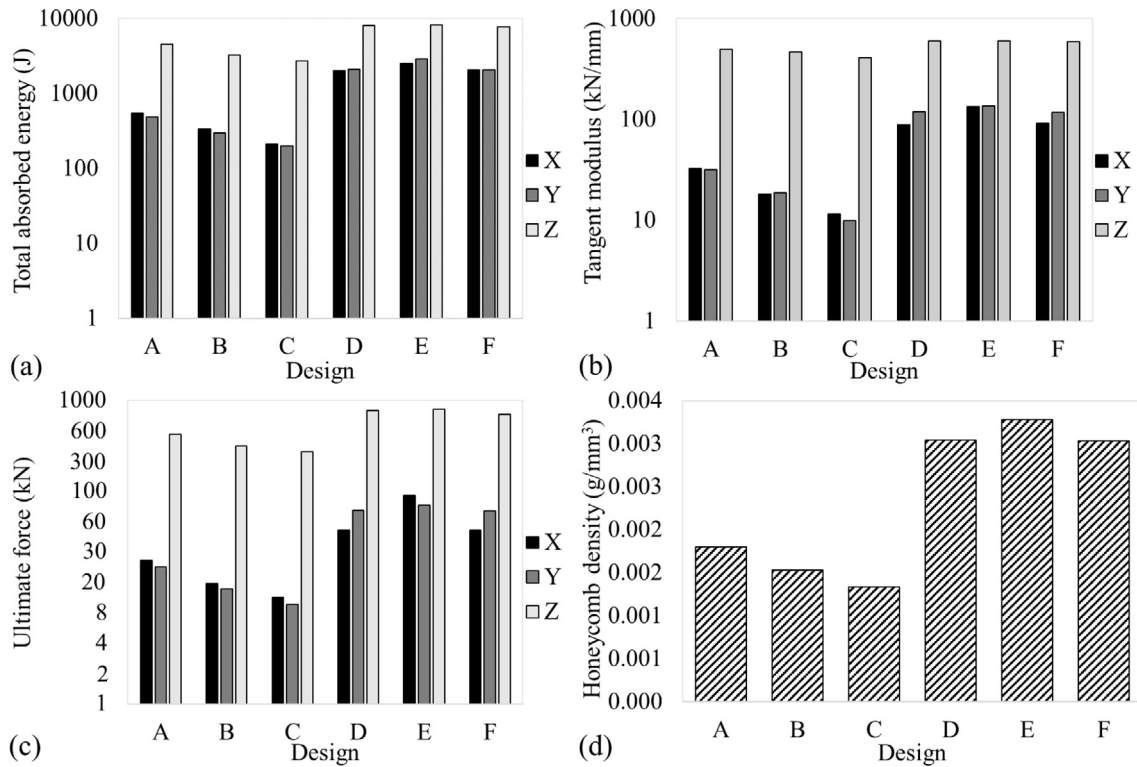
Fig. 20. Comparisons of the key characteristics of the honeycomb structures according to their designs and loading directions (note that the vertical axes are in logarithmic scales except for (d)).
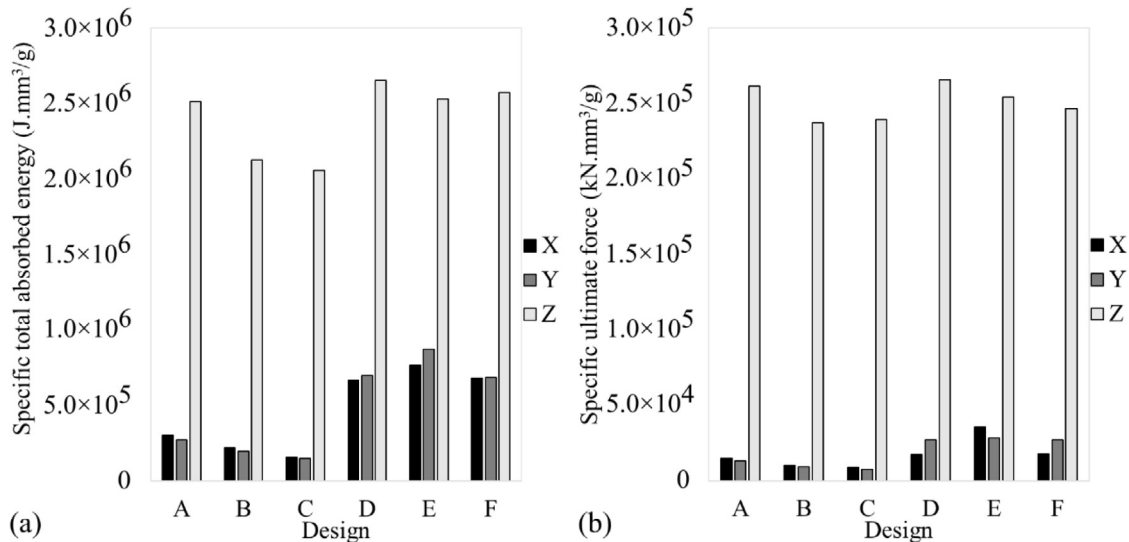

Fig. 21. Comparisons of the specific values of the honeycomb structures according to their designs and loading directions (specific values for each design are calculated based on its ρ_{H} from Table 3).

CRediT authorship contribution statement

Shahriar Afkhami: Writing – review & editing, Writing – original draft, Visualization, Validation, Investigation, Formal analysis, Data curation, Conceptualization. **Mohsen Amraei:** Writing – review & editing, Writing – original draft, Project administration, Methodology, Investigation, Data curation, Conceptualization. **Leroy Gardner:** Writing – review & editing, Writing – original draft, Validation, Methodology, Investigation. **Heidi Piili:** Writing – review & editing, Resources, Funding acquisition. **M. Ahmer Wadee:** Writing – review & editing, Writing – original draft, Validation, Methodology, Investigation. **Antti Salminen:** Writing – review & editing, Resources, Funding acquisition. **Timo Björk:** Writing – review & editing, Supervision, Resources, Methodology, Investigation, Funding acquisition, Conceptualization.

Declaration of competing interest

The authors declare that they have no known competing financial interests or personal relationships that could have appeared to influence the work reported in this paper.

Data availability

Data will be made available on request.

References

[1] M. Moradi, S. Meiabadi, A. Kaplan, 3D printed parts with honeycomb internal pattern by fused deposition modelling; experimental characterization and production optimization, Met. Mater. Int. 25 (2019) 1312–1325, http://dx.doi.org/10.1007/s12540-019-00272-9.

[2] P. Kuznetsov, A. Deev, M. Staritcyn, A. Zhukov, V. Bobyr, Energy absorbing properties of the cellular structures with different wall thickness, produced by the selective laser melting, Mater. Sci. Forum. 933 (2018) 330–336, http://dx.doi.org/10.4028/www.scientific.net/MSF.933.330.

[3] M. Spratt, S. Anandan, R. Hussein, J.W. Newkirk, K. Chandrashekhara, M. Heath, M. Walker, Build accuracy and compression properties of additively manufactured 304 L honeycombs, Rapid Prototyp. J. 26 (2020) 1049–1057, http://dx.doi.org/10.1108/RPJ-08-2018-0201.

[4] A. Kanyilmaz, A.G. Demir, M. Chierici, F. Berto, L. Gardner, S.Y. Kandukuri, P. Kassabian, T. Kinoshita, A. Laurenti, I. Paoletti, A. du Plessis, S.M.J. Razavi, Role of metal 3D printing to increase quality and resource-efficiency in the construction sector, Addit. Manuf. 50 (2022) 102541, http://dx.doi.org/10.1016/j.addma.2021.102541.

[5] J. Ye, P. Kyvelou, F. Gilardi, H. Lu, M. Gilbert, L. Gardner, An end-to-end framework for the additive manufacture of optimized tubular structures, IEEE Access 9 (2021) 165476–165489, http://dx.doi.org/10.1109/ACCESS.2021.3132797.

[6] S. Afkhami, E. Dabiri, K. Lipiäinen, H. Piili, T. Björk, Effects of notch-load interactions on the mechanical performance of 3D printed tool steel 18Ni300, Addit. Manuf. 47 (2021) 102260, http://dx.doi.org/10.1016/J.ADDMA.2021.102260.

[7] S. Afkhami, M. Dabiri, S.H. Alavi, T. Björk, A. Salminen, S. Habib Alavi, T. Björk, A. Salminen, Fatigue characteristics of steels manufactured by selective laser melting, Int. J. Fatigue 122 (2019) 72–83, http://dx.doi.org/10.1016/j.ijfatigue.2018.12.029.

[8] S. Xie, H. Li, C. Yang, S. Yao, Crashworthiness optimisation of a composite energy-absorbing structure for subway vehicles based on hybrid particle swarm optimisation, Struct. Multidiscip. Optim. 58 (2018) 2291–2308, http://dx.doi.org/10.1007/s00158-018-2022-3.

[9] U. Shah, R.K. Kapania, Failure of alternate honeycomb core sandwich panels, in: AIAA Scitech 2019 Forum, American Institute of Aeronautics and Astronautics, Reston, Virginia, Virginia, 2019, http://dx.doi.org/10.2514/6.2019-0206.

[10] A. Antolak-Dudka, P. Płatek, T. Durejko, P. Baranowski, J. Małachowski, M. Sarzyński, T. Czujko, Static and dynamic loading behavior of Ti6Al4V honeycomb structures manufactured by laser engineered net shaping (LENSTM) technology, Materials 12 (2019) 1225, http://dx.doi.org/10.3390/MA12081225, 2019, Vol. 12, Page 1225.

[11] S.Z. Khan, S.H. Masood, R. Cottam, Mechanical properties in tensile loading of H13 re-entrant honeycomb auxetic structure manufactured by direct metal deposition, MATEC Web Conf. 34 (2015) 01004, http://dx.doi.org/10.1051/MATECCONF/20153401004.

[12] M. Amraei, M. Shahravi, Z. Noori, A. Lenjani, Application of aluminium honeycomb sandwich panel as an energy absorber of high-speed train nose, J. Compos. Mater. 48 (2014) 1027–1037, http://dx.doi.org/10.1177/0021998313482019.

[13] S. Malek, L. Gibson, Effective elastic properties of periodic hexagonal honeycombs, Mech. Mater. 91 (2015) 226–240, http://dx.doi.org/10.1016/j.mechmat.2015.07.008.

[14] P. Baranowski, P. Płatek, A. Antolak-Dudka, M. Sarzyński, M. Kucewicz, T. Durejko, J. Małachowski, J. Janiszewski, T. Czujko, Deformation of honeycomb cellular structures manufactured with laser engineered net shaping (LENS) technology under quasi-static loading: Experimental testing and simulation, Addit. Manuf. 25 (2019) 307–316, http://dx.doi.org/10.1016/j.addma.2018.11.018.

[15] S. Anandan, R.M. Hussein, M. Spratt, J. Newkirk, K. Chandrashekhara, H. Misak, M. Walker, Failure in metal honeycombs manufactured by selective laser melting of 304 L stainless steel under compression, Virtual Phys. Prototyp. 14 (2019) 114–122, http://dx.doi.org/10.1080/17452759.2018.1531336.

[16] H. Puga, V.H. Carneiro, P. Correira, V. Vieira, J. Barbosa, J. Meireles, Mechanical behavior of honeycomb lattices manufactured by investment casting for scaffolding applications, Proc. Inst. Mech. Eng. L 231 (2017) 73–81, http://dx.doi.org/10.1177/1464420716665414.

[17] L.J. Gibson, M.F. Ashby, G.S. Schajer, C.I. Robertson, The mechanics of two-dimensional cellular materials, Proc. R. Soc. Lond. Ser. A Math. Phys. Eng. Sci. 382 (1982) 25–42, http://dx.doi.org/10.1098/RSPA.1982.0087.

[18] T. Wierzbicki, Crushing analysis of metal honeycombs, Int. J. Impact Eng. 1 (1983) 157–174, http://dx.doi.org/10.1016/0734-743X(83)90004-0.

[19] J. Zhang, M.F. Ashby, The out-of-plane properties of honeycombs, Int. J. Mech. Sci. 34 (1992) 475–489, http://dx.doi.org/10.1016/0020-7403(92)90013-7.

[20] S. Afkhami, H. Piili, A. Salminen, T. Björk, Effective parameters on the fatigue life of metals processed by powder bed fusion technique: A short review, Procedia Manuf. 36 (2019) 3–10, http://dx.doi.org/10.1016/j.promfg.2019.08.002.

[21] R. Palad, Y. Tian, K. Chadha, S. Rodrigues, C. Aranas, Microstructural features of novel corrosion-resistant maraging steel manufactured by laser powder bed fusion, Mater. Lett. 275 (2020) 128026, http://dx.doi.org/10.1016/j.matlet.2020.128026.

[22] Y. Tian, R. Palad, C. Aranas, Microstructural evolution and mechanical properties of a newly designed steel fabricated by laser powder bed fusion, Addit. Manuf. 36 (2020) 101495, http://dx.doi.org/10.1016/j.addma.2020.101495.

[23] J. Zhang, M. Wang, L. Niu, J. Liu, J. Wang, Y. Liu, Z. Shi, Effect of process parameters and heat treatment on the properties of stainless steel CX fabricated by selective laser melting, J. Alloys Compd. 877 (2021) 160062, http://dx.doi.org/10.1016/j.jallcom.2021.160062.

[24] S. Afkhami, V. Javaheri, E. Dabiri, H. Piili, T. Björk, Effects of manufacturing parameters, heat treatment, and machining on the physical and mechanical properties of 13Cr10Ni1.7Mo2Al0.4Mn0.4Si steel processed by laser powder bed fusion, Mater. Sci. Eng. A (2021) 142402, http://dx.doi.org/10.1016/j.msea.2021.142402.

[25] S. Afkhami, V. Javaheri, K. Lipiäinen, M. Amraei, E. Dabiri, T. Björk, Fatigue performance of stainless tool steel CX processed by laser powder bed fusion, Mater. Sci. Eng. A 841 (2022) 143031, http://dx.doi.org/10.1016/j.msea.2022.143031.

[26] S. Afkhami, V. Javaheri, E. Dabiri, H. Piili, T. Björk, Data related to the microstructural identification and analyzing the mechanical properties of maraging stainless steel 13Cr10Ni1.7Mo2Al0.4Mn0.4Si (commercially known as CX) processed by laser powder bed fusion method, Data Br. 41 (2022) 107856, http://dx.doi.org/10.1016/j.dib.2022.107856.

[27] EOS, EOS StainlessSteel CX material data sheet, 2021, https://www.eos.info/03_system-related-assets/material-related-contents/metal-materials-and-examples/metal-material-datasheet/stainlesssteel/material_datasheet_eos_stainlesssteel_cx_premium_en_web.pdf (accessed April 22, 2021).

[28] ASTM E8/ E8M - 16ae1 Standard Test Methods for Tension Testing of Metallic Materials, (n.d.).

[29] A.B. Spierings, M. Schneider, R. Eggenberger, Comparison of density measurement techniques for additive manufactured metallic parts, Rapid Prototyp. J. 17 (2011) 380–386, http://dx.doi.org/10.1108/13552541111156504.

[30] P. Bajaj, A. Hariharan, A. Kini, P. Kürnsteiner, D. Raabe, E.A. Jägle, Steels in additive manufacturing: A review of their microstructure and properties, Mater. Sci. Eng. A 772 (2020) 138633, http://dx.doi.org/10.1016/j.msea.2019.138633.

[31] S. Gorsse, C. Hutchinson, M. Gouné, R. Banerjee, Additive manufacturing of metals: a brief review of the characteristic microstructures and properties of steels, Ti-6Al-4V and high-entropy alloys, Sci. Technol. Adv. Mater. 18 (2017) 584–610, http://dx.doi.org/10.1080/14686996.2017.1361305.

[32] H. Fayazfar, M. Salarian, A. Rogalsky, D. Sarker, P. Russo, V. Paserin, E. Toyserkani, A critical review of powder-based additive manufacturing of ferrous alloys: Process parameters, microstructure and mechanical properties, Mater. Des. 144 (2018) 98–128, http://dx.doi.org/10.1016/J.MATDES.2018.02.018.

[33] G.W. Hunt, M.A. Peletier, A.R. Champneys, P.D. Woods, M.A. Wadee, C.J. Budd, G.J. Lord, Cellular buckling in long structures, Nonlinear Dynam. 21 (2000) 3–29, http://dx.doi.org/10.1023/A:1008398006403, 2000 211.

[34] J. Burke, E. Knobloch, Homoclinic snaking: Structure and stability, Chaos 17 (2007) 037102, http://dx.doi.org/10.1063/1.2746816.

[35] G.W. Hunt, G.J. Lord, A.R. Champneys, Homoclinic and heteroclinic orbits underlying the post-buckling of axially-compressed cylindrical shells, 1999, pp. 285–297, http://dx.doi.org/10.1142/9789812814876_0014.

[36] M.A. Wadee, R. Edmunds, Kink band propagation in layered structures, J. Mech. Phys. Solids 53 (2005) 2017–2035, http://dx.doi.org/10.1016/J.JMPS.2005.04.005.

[37] M.A. Wadee, L. Gardner, Cellular buckling from mode interaction in I-beams under uniform bending, Proc. R. Soc. Lond. Ser. A Math. Phys. Eng. Sci. 468 (2012) 245–268, http://dx.doi.org/10.1098/RSPA.2011.0400.

[38] M.A. Wadee, L. Bai, Cellular buckling in I-section struts, Thin-Walled Struct. 81 (2014) 89–100, http://dx.doi.org/10.1016/J.TWS.2013.08.009.

[39] M.A. Wadee, M. Farsi, Cellular buckling in stiffened plates, Proc. R. Soc. Lond. Ser. A Math. Phys. Eng. Sci. 470 (2014) http://dx.doi.org/10.1098/RSPA.2014.0094.